



HAL
open science

Biases and improvements in three dynamical downscaling climate simulations over China

Hao Yang, Zhihong Jiang, Laurent Li

► **To cite this version:**

Hao Yang, Zhihong Jiang, Laurent Li. Biases and improvements in three dynamical downscaling climate simulations over China. *Climate Dynamics*, 2016, 47 (9), pp.3235-3251. 10.1007/s00382-016-3023-9 . hal-01416309

HAL Id: hal-01416309

<https://hal.sorbonne-universite.fr/hal-01416309>

Submitted on 14 Dec 2016

HAL is a multi-disciplinary open access archive for the deposit and dissemination of scientific research documents, whether they are published or not. The documents may come from teaching and research institutions in France or abroad, or from public or private research centers.

L'archive ouverte pluridisciplinaire **HAL**, est destinée au dépôt et à la diffusion de documents scientifiques de niveau recherche, publiés ou non, émanant des établissements d'enseignement et de recherche français ou étrangers, des laboratoires publics ou privés.

1 **Biases and Improvements in three Dynamical Downscaling**
2 **Climate Simulations over China**

3
4 Hao Yang^{1,2} • Zhihong Jiang¹ • Laurent Li³

5
6 **Abstract:** A dynamical downscaling is performed to improve the regional climate
7 simulation in China. It consists of using a variable resolution model LMDZ4 nested
8 into three global climate models (GCMs): BCC-csm1-1-m, FGOALS-g2 and
9 IPSL-CM5A-MR, respectively. The regional climate from different simulations is
10 assessed in terms of surface air temperature and rainfalls through a comparison to
11 observations (both station data and gridded data). The comparison includes climatic
12 trends during the last 40 years, statistical distribution of sub-regional climate, and the
13 seasonal cycle. For surface air temperature, a significant part of the improvement
14 provided by LMDZ4 is related to the effect of surface elevation which is more
15 realistic in high-resolution simulations; the rest is related to changes in regional or
16 local atmospheric general circulation. All GCMs and the downscaling model LMDZ4
17 are, more or less, able to describe the spatial distribution of surface air temperature
18 and precipitation in China. LMDZ4 does show its superiority, compared to GCMs, in
19 depicting a good regional terrain including the Tibetan Plateau, the Sichuan Basin and
20 the Qilian Mountains.

21 **Accepted manuscript for Climate Dynamics, Feb. 2016**

1. Key Laboratory of Meteorological Disaster of Ministry of Education, Collaborative Innovation Center on Forecast and Evaluation of Meteorological Disasters, Nanjing University of Information Science and Technology, Nanjing, China

2. Hubei Key Laboratory for Heavy Rain Monitoring and Warning Research, Institute of Heavy Rain, China Meteorological Administration, Wuhan, China

3. Laboratoire de Météorologie Dynamique, CNRS/UPMC, Paris, France

Hao Yang, E-mail: yanghao0202@126.com

Corresponding Author: Zhihong Jiang, E-mail: zhjiang@nuist.edu.cn

Laurent Li, E-mail: laurent.li@lmd.jussieu.fr

22 1. Introduction

23 Numerical modeling is one of the most effective tools for climate change
24 researches. There are more than 40 global models participating in the Coupled Model
25 Intercomparison Project phase 5 (CMIP5) (Taylor et al. 2012) which provides a large
26 number of climate simulations. Compared to the previous exercise CMIP3, the ability
27 of simulating historical climate at global scale has been largely enhanced (Taylor et al.
28 2012; Sperber et al. 2012). However, the ability of simulating climate at regional scale
29 is still poor, in particular for rainfall (Kitoh et al. 2013; Jiang et al. 2015).

30 China, located in the East Asian monsoon area, is one of the regions in the world
31 possessing large climate variability. A complex surface topography also increases the
32 difficulties for GCMs to accurately simulate the regional climate (Sperber et al. 2012).
33 The main reason arises from their low spatial resolution, not capable of considering
34 regional scale forcing, such as the complex terrain. The heterogeneity of surface
35 conditions generally makes regional climate simulations unreliable. This is
36 particularly true for the Tibetan Plateau and the surrounding areas (Mannig et al.
37 2013). To get higher-resolution and good-quality data, downscaling is indispensable
38 (van Vuuren et al. 2011; Gao et al. 2010; Chen et al. 2011a; Jiang et al. 2012; Guo et
39 al. 2012; Guo et al. 2014).

40 The technique of dynamical downscaling generally consists of using a
41 high-resolution regional model nested into global models. It ensures a complete
42 coherence among different variables. With a refined terrain, the capability of the
43 regional model in simulating local weather and climate can be significantly improved
44 (Giorgi et al. 2004; Frei et al. 2006). Based on this dynamical downscaling
45 methodology, a few investigations on regional climate over China have been reported
46 (Shi et al. 2011; Zhang 2012; Gao et al. 2012; Wang et al. 2013). However, there is
47 still a lack of downscaling studies with multi-model global forcing, obviously due to
48 the large demand on computer resources.

49 An alternative to the limited-area modeling is to generate regional climate
50 information with variable-resolution (zoomed) global atmosphere general circulation
51 models, the higher-resolution domain being put over the region of interest (Deque and
52 Piedelievre 1995; Goubanova and Li 2007). Such a global model can also work as a
53 traditional limited-area model if the whole globe outside the interested domain is
54 considered as buffer zone which is driven by re-analysis data or 6-hourly outputs of
55 global ocean-atmosphere coupled models. Such a regional configuration apparently
56 wastes computer resources, the buffer zone where nudging takes place covering the

57 whole globe. But this over-consumption is generally tolerable, since the number of
58 model grids outside the interested domain is relatively limited if the zoom is
59 appropriately designed. The advantage of this regional modelling approach resides in
60 its general universality for different regions on Earth. LMDZ4, developed in the
61 Laboratoire de Météorologie Dynamique, France, is a variable-grid GCM with the
62 possibility of zooming and nudging. Many applications have been reported for
63 different regions of the world: the Mediterranean (Li 2006, Rojas et al. 2013;
64 L'Heveder et al. 2013; Vautard et al. 2013); South America (Carril et al. 2012; Solman
65 et al. 2013). Regional applications were also reported over East Asia (Zou et al. 2010;
66 Chen et al. 2011a).

67 As part of the Coordinated Regional Climate Downscaling Experiment
68 (CORDEX) project (Giorgi et al. 2009), we simulate and analyze regional climate
69 change signals over China under different scenarios. The particularity of our study is
70 to use LMDZ-regional to conduct an ensemble of climate downscaling simulations
71 with outputs of many global models (three when the paper was written). Simulations
72 cover present day (1961–2005) and future (2006–2100) for RCP4.5 and RCP8.5 IPCC
73 scenarios (Taylor et al. 2012). We hope that the multi-model ensemble approach
74 allows us to deal with the issue of uncertainty by examining the spread of results.

75 In this paper, we describe results from LMDZ4 nested into three CMIP5 global
76 simulations. Section 2 describes the model and data used. In section 3.1 to 3.3, the
77 simulation performance between global models and their counterparts after
78 downscaling is compared. Section 3.4 presents a simple off-line bias-correction
79 method applied to surface air temperature, by revising the surface elevation in global
80 models and LMDZ4. We believe that this correction, directly related to surface terrain,
81 is meaningful for impact studies that might need high quality in surface air
82 temperatures. Since there is no simple methodology allowing a bias correction for
83 precipitations, the added value of regional simulations is much clearer for
84 precipitations.

85 **2. Model description and data**

86 LMDZ4 used in this study (Le Treut et al. 1994; Li 1999), is zoomed in East Asia
87 (zoom center at 30°N/110°E, coverage 5°~55°N, 85°~135°E). There are 120×120
88 latitude and longitude grids and 19 layers in the vertical. The spatial resolution inside
89 the zoom is approximately 0.6°×0.6°. The driving forcing is added through a
90 relaxation procedure. We put a long (10 days, but not infinite, to be comparable with

91 other simulations using this historical set-up) relaxation time scale inside the zoom,
92 while the relaxation time scale is 1.5 hours outside. The use of two distinct relaxation
93 time scales inside and outside implies that the model runs almost freely inside the
94 zoom, whereas it totally follows the forcing outside the zoom. This operation (a long
95 but finite time scale inside the zoom) has some similarities with the concept of
96 spectral nudging commonly used in limited-area models for climate downscaling. But
97 our nudging effect is very weak, and we just interpolate (with a bi-linear algorithm)
98 global fields into the regional grid without performing any scale filtering. The main
99 physical processes used in the model correspond to the atmospheric component of the
100 IPSL-CM5A coupled model, as described in Hourdin et al. (2006) and Dufresne et al.
101 (2013).

102 The three global climate models (GCMs) that we used as drivers are all from the
103 5th Coupled Model Intercomparison Project (CMIP5) (Taylor et al. 2012).
104 BCC-CSM1.1-m is the climate system model developed by the China Meteorological
105 Administration, National Climate Center (Wu et al. 2013). FGOALS-g2 was
106 developed by the Institute of Atmospheric Physics, State Key Laboratory of
107 Numerical Modeling for Atmospheric Sciences and Geophysical Fluid Dynamics
108 (IAP-LASG), China (Li et al. 2013). FGOALS-g2 was obviously improved in many
109 aspects in comparison with early versions of FGOALS (Zhou et al. 2013; Yu et al.
110 2013). The performance of the two models has been evaluated in Zhou et al. (2014).
111 IPSL-CM5A-MR is the last version of the global climate model developed by IPSL
112 (Institute Pierre-Simon Laplace), France, taking part in different CMIP exercises. It
113 generally gives a good performance at global scale or in East Asia (Chen et al. 2011a).
114 The three selected models are quite representative of the climate modelling
115 community. They are considered as suitable for studies of Southeast Asian climate,
116 consensus obtained from many published works on global models evaluation (Sperber
117 et al. 2013; Kitoh et al. 2013; Zhou et al. 2014; Jiang et al. 2015). LMDZ4 used in this
118 study is the atmospheric circulation module in IPSL-CM5A-MR, but with different
119 horizontal and vertical resolution.

120 LMDZ4 is used in its regional configuration, its main variables being nudged to
121 6-hourly outputs of GCMs. It is actually used as a traditional limited-area model with
122 the whole globe as buffer zone that receives outputs of GCMs. The nudged variables
123 include zonal wind, meridional wind, temperature and specific humidity, with a time
124 interval of 6 hrs. The SST and sea ice prescribed as surface boundary conditions in the
125 simulation are also from GCMs. The effective time period covers 1961-2005. Our

126 downscaling approach is the largely-used one-way nesting technique, which means
127 that there is no feedback to GCMs from the regional model. Results after downscaling
128 are referred to as LMDZ/BCC, LMDZ/FGOALS and LMDZ/IPSL in this paper.

129 For the purpose of model assessment, daily temperature and rainfall at a few
130 meteorological stations in China are used. They are quality checked and homogenized
131 as described in Xu et al. (2009) and Chen et al. (2010). These two data sets are
132 available with a resolution of $0.5^{\circ}\times 0.5^{\circ}$, for the same time period (1961-2005) of
133 model runs. The topography of meteorological stations is provided by China
134 Meteorological Administration (CMA). Main characteristics of models and observed
135 data sets are listed in Table 1. The original resolution of models is preserved in the
136 following analysis.

137 Fig. 1 shows the spatial resolution and surface height in different models (LMDZ,
138 BCC, FGOALS and IPSL) in East Asia. The region roughly follows a three-step
139 orography from east to west. The first step is the coastal plain and some hilly ground,
140 with altitude lower than 500 m. The second step comprises regions with mountains
141 and hills, roughly from 500 to 3000 m. The third step mainly refers to the Tibetan
142 Plateau with altitudes over 3000 m. LMDZ is characterized by a higher resolution in
143 comparison with the other three global models. It can give more accurate coastlines
144 and terrains. The structures of the Wuyi Mountains (Southeast China costs), the Qilian
145 Mountains (in the north of the Tibetan Plateau, oriented from Southeast to Northwest),
146 the Qaidam Basin (between the Tibetan Plateau and the Qilian Mountains), and the
147 Sichuan Basin (in the east of the Tibetan Plateau) are all clearly visible and well
148 depicted in the downscaling model. The Tarim Basin (between the Tibetan Plateau
149 and the Tianshan Mountains) and the Junggar Basin (between the Tianshan and Altai
150 Mountains) are at the western boundary of our zoom domain.

151 **3. Results and analysis**

152 **3.1 Temperature and Precipitation mean climatology**

153 Surface air temperature will be first assessed. By examining the surface air
154 temperature among the three global models and their counterparts after downscaling,
155 we can see that all of them are well consistent with the observation. Temperature in
156 China is strongly affected by terrains (as shown in Fig. 2). For example, the
157 observational temperature around the Sichuan Basin is approximately 15°C or more,
158 which is evidently higher than the surrounding areas (roughly $12\sim 15^{\circ}\text{C}$).

159 Compared with observations, GCMs reproduce well the patterns of temperature

160 decrease from south to north (Fig. 2). The pattern correlation coefficients between
161 simulated and observed annual-mean temperature are 0.94, 0.92 and 0.96, respectively,
162 for BCC, FGOALS and IPSL (as shown in Fig. 2a). The root-mean-square errors
163 (RMSE) are 3.4°C, 4.7°C, and 2.3°C, respectively (Fig. 2b). However, GCMs show a
164 weak skill of simulation in the Sichuan Basin. This is particularly true for FGOALS
165 which does not show the warm center at all. The downscaling results show a
166 significant improvement for the Sichuan Basin and other mountainous regions. The
167 high-value center in the Qaidam Basin and the low-value center in the Qilian
168 Mountains and the Tarim Basin are obviously better achieved after downscaling than
169 those in GCMs. This improvement is a direct consequence of the higher-resolution
170 terrain and consistent with previous works (Deque 1995; Gao et al. 2010; Shi et al.
171 2011; Mannig et al. 2013). Similarly, topographic structures of LMDZ4 are very well
172 reflected in the temperature patterns, much better than in GCMs. The pattern
173 correlation coefficients between downscaled and observed annual-mean temperature
174 are increased to 0.98, 0.97 and 0.98, respectively, for BCC, FGOALS and IPSL. The
175 RMSE are decreased to 2.6°C, 3.6°C, and 2.0°C, respectively.

176 Precipitation is another important climate variable to evaluate. China experiences
177 a typical monsoon climate and large rainfall variability in both space and time.

178 As revealed in observation data (Fig. 3), the annual mean precipitation in China
179 decreases from the southeast coast to the northwest. In east China, the 3 mm/day
180 rainfall intensity reaches 32°N. The three GCMs can basically depict the main
181 characteristics of rainfall distribution with a gradual decrease from east to west, but
182 important biases can be noted. The spatial pattern correlation coefficients between
183 simulated and observed precipitation are of 0.61, 0.59 and 0.62, respectively, for BCC,
184 FGOALS and IPSL (as shown in Fig. 3a). The RMSE are 1.19, 1.15, and 1.21
185 (mm/day), respectively (Fig. 3b). In BCC and IPSL, the simulated precipitation in
186 southeast of the Tibetan Plateau is stronger than observation, while much less in
187 southeast China and the Sichuan Basin. FGOALS simulates more precipitation on the
188 Tibetan Plateau and in the Sichuan Basin. These precipitation defects are common in
189 GCM simulations with coarse resolution (Li et al. 2011; Chen et al. 2011b; Jiang et al.
190 2012).

191 After downscaling, there is a significant improvement in the regions mentioned
192 above. In particular, a high-value center in the Qilian Mountains has been reproduced
193 as the observation shows. The pattern correlation coefficients between downscaled
194 and observed precipitation are increased to 0.67, 0.65 and 0.69, respectively, for BCC,

195 FGOALS and IPSL. The RMSE are decreased to 1.03, 0.98, and 1.16 (mm/day),
196 respectively. Both LMDZ/BCC and LMDZ/IPSL reduce the wet biases around
197 northeast China and the Tibetan Plateau. LMDZ/FGOALS also improves the
198 simulated ability in east of the Tibetan Plateau. Moreover, the dry bias of GCMs in
199 southeast China has been reduced after downscaling.

200 We examine furthermore models performance in different months of the year.
201 Figure 4 displays the spatial correlation coefficient and RMSE in function of month.
202 For surface air temperature (Fig. 4, panels a and c), the correlation coefficient is
203 generally smaller in summer than in winter; the RMSE does not show large variation
204 during the year. There is a general improvement in regional simulations than in global
205 models. FGOALS seems the less skillful for the two parameters. For precipitation
206 (Fig. 4, panels b and d), both the correlation coefficient and RMSE are smaller in
207 winter than in summer, due to the fact that this region is generally dry in winter and
208 wet in summer.

209 In summary, the dynamical downscaling shows a significant improvement in the
210 spatial distribution of both temperature and precipitation. The main patterns of
211 temperature and precipitation over China are well depicted in the downscaling
212 simulations. This is mainly due to a detailed terrain present in LMDZ4 for the Tibetan
213 Plateau, the Sichuan Basin and the Qilian mountains.

214 3.2 Climatic trends

215 The long-term trend of a climate variable can be calculated with a simple linear
216 regression. It consists of calculating the regression coefficient of the climate time
217 series (temperature or precipitation) against a regularly-increasing time series
218 $\{t=1,2,\dots,n\}$.

$$219 \quad a_x = r_x (\sigma_x / \sigma_t) \quad (1)$$

220 where r_x denotes the correlation coefficient between the two time series, σ_x , σ_t are
221 their respective standard deviation. The statistical significance of r_x can be calculated
222 by a t-test.

223 The global climate was dominated by a warming trend in the 20th century
224 (Taylor et al. 2012). Fig. 5 shows the spatial distribution of the trend evaluated from
225 1961 to 2005 with the annual-mean temperatures, for observations and different
226 models respectively. Observational field presents an increasing trend of temperature
227 in most of the country. The temperature increases much faster in the north than in the
228 south. The warming rate in south China is lower than $0.2^\circ\text{C}\cdot(10\text{a})^{-1}$, but that in the

229 north can exceed $0.4^{\circ}\text{C}\cdot(10\text{a})^{-1}$, with stronger intensity in Inner Mongolia, northeast
230 China and east of the Tarim Basin. The observed temperature pattern is almost
231 reproduced in the global models of BCC and FGOALS, but the amplitude is much
232 lower than that in observation, and the high-value centers are not well depicted. The
233 spatial distribution given by IPSL is characterized by over-estimated values in south
234 China. Meanwhile, the significant warming in Northeast China does not appear.

235 After downscaling, the spatial patterns of trend in the three models are more
236 precisely displayed. The spatial distribution of lower-in-the-south and
237 higher-in-the-north is more consistent with observation. But the warming rate is larger
238 in simulations than in observation, particularly in Northeast China, where the
239 warming rate exceeds $0.6^{\circ}\text{C}\cdot(10\text{a})^{-1}$. Simulated trends in central and south China in
240 LMDZ/BCC and LMDZ/IPSL are also higher than their counterparts in observation.

241 Observed trend of annual-mean precipitation from 1961 to 2005 shows a decrease
242 over North China, but an increase in the middle and lower reaches of the Yangtze
243 River and in the coastal areas of south China (as shown in Fig. 6). This result is in a
244 general agreement with previous studies which show a contrasting pattern of
245 precipitation trend in east China: wet in the south and dry in the north (Zou et al.
246 2010).

247 The ability of models in simulating precipitation is generally weaker than that in
248 simulating surface air temperature. Simulated trend for precipitation is still far from
249 realistic, although the situation for temperature is more consistent with observation
250 (shown in Fig. 6). Results from different GCMs all revealed a sharp increase in north
251 China, but a decrease in the Yangtze-Huaihe river basin, especially for FGOALS and
252 IPSL, which are almost contrary to the observation. Compared to the previous
253 exercise in CMIP3, the ability of simulating interannual variability and seasonal cycle
254 of East Asian summer monsoon has been largely enhanced in CMIP5 (Sperber et al.
255 2012; Flato et al. 2013). However, for rainfall, there are still important uncertainties
256 and differences among GCMs (Jiang et al. 2013; Zhang et al. 2013). After
257 downscaling, all the three models show a gradually decreasing trend of precipitation
258 in north China, but still significantly different from observation. LMDZ/IPSL
259 reproduces the increasing trend in the Yangtze-Huaihe drainage basins. It performs
260 much better than IPSL, its counterpart of global models.

261 Figures 5 and 6 show an obvious advantage for LMDZ4. The regional
262 simulations are closer to each other than to the respective driving GCMs. For example,
263 the three downscaled simulations show a meridional gradient of warming in line with

264 observations, while the driving GCMs miss it completely (Fig. 5). Similar
265 phenomenon for the precipitation trends (Fig. 6). Trend patterns in the regional runs
266 are generally different from those in GCMs, but closer to each other. That is because,
267 in our experiment, LMDZ4 conducts quite freely inside the target area ($5^{\circ}\sim 55^{\circ}\text{N}$,
268 $85^{\circ}\sim 135^{\circ}\text{E}$) with very weak forcing from GCMs. The relaxation time scale is 10 days
269 inside the entire zoom. This corresponds to a week nudging used in some limited-area
270 models. So the three downscaled simulations are more resemblant to each other than
271 to their respective driving GCMs.

272 Based on the above comparative studies before and after the downscaling, there
273 is an impressive ability for temperature, but feeble skill in GCMs for the simulated
274 precipitation. Moreover, for both surface air temperature and precipitation, the good
275 regions for climate means are not necessarily the good areas for trends.

276 3.3 Validation in sub-regions

277 Due to significant regional differences of climate in China, it is useful to divide
278 China into a few sub-regions. The regional division is shown in Fig.1a for 6
279 sub-regions, reflecting the increasing continental characteristics of climate from east
280 to west, as well as the south-north gradient and the main orographic features. The
281 sub-regions are Northeast China (NE), North China (NC), Yangtze river basin (YZ),
282 Southeast China (SE), Southwest China (SW) and Northwest China (NW).

283 Unlike for long-term trend, it is not relevant to compare simulated sequences
284 against observed ones, especially for the interannual time scale. However, it is
285 adequate to compare their statistical behaviors from each other. Figure 7 shows such
286 statistical properties (in the form of box-and-whisker plots) of annual-mean
287 temperature during the period 1961-2005. Each panel shows the area average of the
288 corresponding sub-region.

289 On the whole, the medians (quantity separating the higher half from the lower
290 half of the distribution) of GCMs and downscaling runs are generally smaller than
291 that of the observation, which indicates a cold bias in most regions, except in NC and
292 SE. In NE, NW and SW, the median temperatures in downscaling runs are more
293 accurate than those in GCMs. The median temperatures in downscaling runs in NE,
294 YZ and SE are closer to observation than those in other sub-regions, and the median
295 biases are smaller than 2°C . We can however see that, the minimum and maximum
296 values (represented by the whiskers) in simulated temperatures do not show
297 significant changes after the downscaling.

298 Compared to temperature, rainfall in the dynamical downscaling simulation has a
299 more obvious positive effect (Figure 8), especially in NE, NW and SW. The wet
300 biases in GCMs over most areas range from 20% to 100%, with some areas exceeding
301 150%. The downscaled rainfalls have a reduced bias in median values. Both GCMs
302 and regional simulations have a wet bias in west areas with complex terrain. Earlier
303 studies have shown that the reason lies within the upwind effect, which is even
304 stronger with a better-resolved topography (Mannig et al. 2013). It should be noted
305 that rainfall simulation in climate models is still an issue of grand challenge, since
306 there are many processes controlling the macro-properties and micro-physics of
307 clouds and precipitations, but missing in current parameterizations. Moreover, the
308 lack of a high-quality and high-resolution observed rainfall dataset contributes to the
309 persistency of uncertainties in models, and makes models evaluation a very
310 challenging issue (You, 2012) .

311 China, strongly affected by the East Asian Monsoon, presents a strong seasonal
312 cycle in both temperature and rainfall. Therefore, it is necessary to evaluate the
313 simulation capacity of GCMs and downscaling models in terms of seasonal changes.
314 Figure 9 shows the seasonal cycle of temperature in different regions from
315 observation, GCMs and downscaled simulations respectively. It can be learned that,
316 the maximum temperature difference between summer and winter appears in
317 Northeast, approaching 40°C. The primary cause is its high-latitude location, where
318 under the control of the Siberia cold high-pressure in winter, the temperature is as low
319 as -20°C, while in summer it exceeds 20°C because of the East Asian summer
320 monsoon. In North China, models present a relatively small deviation. They are close
321 to the observation. All the simulated temperatures in the Yangtze River basin are
322 higher in summer and lower in winter than the observation. Southeast China has a
323 similar situation except that the temperature in LMDZ/FGOALS has a cold bias all
324 year round. Temperatures among most models in Northwest and Southwest are lower
325 throughout the year, except for some models (LMDZ/BCC and LMDZ/IPSL) showing
326 higher temperature in summer. All downscaled results are closer to observation than
327 GCMs. For all sub-regions, whatever GCMs or downscaled simulations, September
328 and October show the best performance.

329 For precipitation, the seasonal cycles from different regions show a broad range
330 of characteristics (see Fig. 10). A common behavior is, however, that rainfalls peak in
331 summer for all sub-regions. Northeast and North China show the most remarkable
332 seasonal cycle with peaks in July, accompanied with rapid transitions in June and

333 August (Fig. 10, NE and NC). All simulations seem able to reproduce such
334 characteristics in these two regions. But they have a general dry bias in summer,
335 while a wet bias in other seasons. IPSL in Northeast China and FGOALS in North
336 China are exceptions, showing smaller deviations after downscaling.

337 In the Yangtze river basin, the observed precipitation peaks in July, while all
338 GCMs and downscaled maxima appear in May with an advance in phase (except for
339 IPSL), and precipitation intensity is weaker in summer, autumn and winter, but
340 stronger in spring. In Southeast China, precipitations peak in June, but most
341 simulations show a phase shift to July or a too-broad distribution from May to August.
342 Precipitation amounts in all simulations are generally smaller than the observed
343 values (see Fig.10 SE).

344 The mountainous regions in Southwest and Northwest China (Fig. 10, SW and
345 NW) with their complex terrain show large differences for each model throughout the
346 year. All the models overestimate precipitation in these two regions, while the three
347 downscaling simulations show significant improvements. This is particularly true for
348 the model FGOALS running with a lower resolution.

349 To quantify the above comparison, we calculate the correlation coefficient and
350 the RMSE for each curve in Fig. 10 with their counterpart from observation (black
351 curve in Fig. 10). Results (Table 2) show that there is a general improvement from
352 GCMs to regional simulations in terms of RMSE, but not always correlation
353 coefficient. This means that LMDZ-regional has a better mean climatology, but its
354 seasonal match, controlled by GCMs, is not ameliorated. We also observe the same
355 results for the surface air temperature (mean climatology improved, but not the
356 seasonal match itself; results not shown).

357 In summary, models show different performances in different sub-regions.
358 Consistent with previous studies (Zhou et al. 2002; Chen et al. 2011; Jiang et al. 2013),
359 most GCMs have a poor skill in terms of precipitation in west China (especially the
360 Tibet Plateau). Encouragingly in our study, for both temperature and precipitation, the
361 dynamical downscaling simulations are generally closer to observations. Among the
362 three GCMs, the downscaling simulation from FGOALS shows the most obvious
363 improvements. For both temperature and rainfall, the superiority of dynamical
364 downscaling is deeply dependent on topography. Especially over the complex terrain
365 in China, the dynamical downscaling has a more powerful capacity than GCMs.

366 **3.4 Orographic effects**

367 Our previous analysis shows clearly that a dynamical downscaling gives
368 important improvements in complex-terrain regions in Southwest and Northwest
369 China. The observational data at meteorological stations can be regarded as the
370 “ground truth”, which help us to examine GCMs and downscaling performances in
371 more details. We select 25 stations covering the transition from wet coastal regions to
372 dry inland areas (see Fig. 11).

373 It can be seen that almost all elevations in GCMs and LMDZ4 are higher than the
374 real elevation. This is due to the fact that terrain in models is of mean topography, but
375 meteorological stations are generally located in valleys or low-land areas. The terrain
376 height deviations (see ΔEL , simulations minus observations) for stations in west
377 China are generally larger. For most stations with low altitude in east China, the
378 surface height in LMDZ4 is closer to observed elevation than GCMs (as shown in
379 Table 3).

380 By comparing temperatures from GCMs and downscaled simulations, it is found
381 that the average temperature bias at the 25 stations is reduced after downscaling, with
382 absolute value 2.53°C in GCMs against 1.13°C in downscaled simulations, except
383 for Fuzhou, Xichang, Kunming and Urumqi (see ΔT). Bias of simulated temperature
384 is usually proportional to the increase of local height. The accuracy of temperature
385 simulation depends on altitudes (Zhao et al. 2008).

386 To investigate quantitatively the topographic effects on simulated temperature,
387 we perform a topographic correction, in a similar way as used in a
388 land-data-assimilation system (Cosgrove et al. 2003). Temperatures from models at
389 each station are adjusted with the following algorithm:

$$390 \quad T_{corr} = T_{sim} + \mu\Delta H \quad (2)$$

391 where T_{cor} is the temperature ($^{\circ}\text{C}$) after correction, and T_{sim} the simulated one ($^{\circ}\text{C}$)
392 before correction; μ is the lapse rate (assumed to be $0.65^{\circ}\text{C}/100\text{m}$), and ΔH the
393 difference of elevations (m) between models and the true topography.

394 Corrections from GCMs and regional simulations are all shown in Table 3 (Δ
395 T-cor). For GCMs, the absolute value of temperature bias after topographic correction
396 is reduced to 1.09°C (against 2.53°C before correction). The temperature bias of the
397 regional simulations is 1.13°C . The bias becomes 0.98°C if the same bias correction is
398 applied. It is evident that, for temperature, the topographic correction plays a role in
399 GCMs as well as in the dynamical downscaling simulations. This correction leads to
400 temperatures closer to the observation. From ΔT and $\Delta T\text{-cor}$, we can also observe
401 that, in western high-altitude stations like Lhasa, Xi’an, Lanzhou, Xining, Yinchuan

402 with strong biases in GCMs, the effects of topographic correction are also more
403 spectacular than that in eastern low-altitude stations like Harbin, Shenyang, Chifeng,
404 Jinan, Nanjing, etc. In agreement with previous studies, our results confirm that the
405 simulated temperature is highly dependent on altitude of model grids and on
406 complexity of model topography. This general behavior should be primarily taken into
407 account for any applications of model outputs to studies of climate change impacts.

408 For precipitations, Table 3 shows that GCMs generally have over-estimations at
409 stations in wet basins in the east, but under-estimations along the western mountain
410 ranges. The average precipitation bias for the 25 stations is reduced after downscaling,
411 with a relative error of 35.8% in GCMs and 28.2% in regional simulations. The
412 amelioration provided by the dynamical downscaling is furthermore revealed different
413 for east and west regions. Some high-altitude stations like Lhasa, Lanzhou, Xining,
414 Yinchuan and Yushu, with serious wet bias in GCMs, have the most significant
415 amelioration after downscaling. Table 3 also reveals that the simulated precipitation
416 deviations are relative to the elevation of stations for both GCMs and downscaling
417 simulations, the higher elevation the larger deviation. Unlike the surface air
418 temperature that can be partly corrected by considering the terrain height,
419 precipitation cannot be simply corrected without considering changes in the regional
420 or local atmospheric general circulation (Tippett et al. 2003).

421 Since surface air temperature and precipitation are strongly controlled by
422 atmospheric circulation, their amelioration in downscaling simulations should be
423 accompanied with amelioration in atmospheric dynamic fields, such as wind and
424 geopotential height (GHT). Figure 12 (left two panels) shows geopotential height at
425 500 hPa and winds at 850 hPa, as depicted in ERA-Interim, for summer and winter
426 respectively. Mean biases of GCMs (middle) and downscaling simulations (right) are
427 also shown. For both summer and winter, there is some resemblance between GCMs
428 and downscaling simulations, due to the nudging relationship between them. This
429 resemblance is found larger in winter than in summer, which can be explained by the
430 fact that winter climate in the region is much more controlled by large-scale
431 circulation in comparison to summer regional climate. Many regional events can
432 develop in summer without necessarily a corresponding large-scale structure,
433 especially when convection is dominant .

434 Let us now examine further the summer situation. The GCMs bias is consistent
435 with a general imperfection in many models, with a too-strong south wind system in
436 East China, making the summer monsoon too much inland. This bias is largely

437 reduced in downscaling simulations. We believe that the amelioration of atmospheric
438 circulation in the downscaling simulation brings a significant improvement for both
439 surface air temperature and precipitation.

440 In summary, because the downscaling model LMDZ4 has a higher resolution and
441 a more accurate representation of the underlying terrain, surface air temperature is
442 generally better in LMDZ4 than in GCMs. The topographic correction plays a role in
443 GCMs as well as in the dynamical downscaling simulations. However, the orographic
444 effect is not the only reason why the dynamical downscaling performs better, the
445 amelioration of the atmospheric general circulation at regional or local scale certainly
446 plays its role.

447 Our results are consistent with those presented in Gao et al. (2006) who studied
448 the performance of a limited-area climate model running over East Asia, in function
449 of different model horizontal resolutions. They also tried to isolate the topographic
450 effect from that of the resolution. They showed that the first contributor for a better
451 simulation of precipitation in East Asia is the increase of model resolution. This
452 resolution effect is more important than that from a better description of the surface
453 topography which is only a second contributor.

454 **4. Summary and Conclusion**

455 Three global models, BCC-csm1-1-m, FGOALS-g2 and IPSL-CM5A-MR, were
456 used to drive a variable grid atmospheric general circulation model LMDZ4, to
457 produce an ensemble of dynamical downscaling simulations in East Asia. Simulations
458 cover the present-day period (1961–2005). The research in this study is, primarily, of
459 practical significance for developing and validating suitable regional climate model
460 system in eastern China. The performance of GCMs and downscaling simulations has
461 been evaluated in terms of precipitation and surface air temperature in China. We
462 compared their mean climatology and long-term trend.

463 In general, GCMs and downscaling models are all able to reproduce the main
464 spatial patterns of temperature and precipitation over China. Compared to GCMs, the
465 intensity and location of simulated temperature and precipitation from LMDZ4 are
466 closer to observations. The spatial pattern correlation coefficient calculated for the
467 annual-mean temperature varies from 0.92/0.94 in GCMs to 0.97/0.98 in downscaling
468 simulations. The same indicator for rainfall varies from 0.59/0.62 to 0.67/0.69. The
469 root mean square errors also significantly decrease from GCMs to regional
470 simulations for both temperature and precipitation. The downscaling with FGOALS

471 exhibits the most significant improvement, compared with BCC and IPSL. This is due
472 to the fact that FGOALS has the lowest spatial resolution and the downscaling shows
473 its most visible added-value.

474 For long-term trend from 1961 to 2005, a general warming is observed over
475 China with minimum amplitude near the coasts and stronger amplitude inland. All
476 GCM and regional simulations catch the warming trend. But the spatial patterns are
477 not always consistent with the observed one. For rainfall, there is a dipole structure in
478 East China: wet conditions in the south and dry conditions in the north. This structure
479 does not seem to be reproduced, neither in GCMs nor in regional simulations. We
480 note however that the three regional runs present some similar structures, although
481 their counterpart in GCMs is quite different: dry in Northeast China and South China,
482 but weak wet conditions in North China. Simulation in precipitation tendency was
483 inferior to that in temperature. Deficiency in the trend simulation has received more
484 and more concerns in climate models currently (Wang et al. 2013; Dong et al. 2013;
485 Dong and Zhou. 2013). That requires the comparison of multi-GCM or RCM
486 ensembles (Gao et al. 2012b). The CORDEX project which we are taking part in will
487 help to understand uncertainties of climate changes including both historical period
488 and future projections (Giorgi et al. 2009).

489 We also divided China into 6 sub-regions and investigated the statistical
490 properties of regional-mean temperature and precipitation. Results are displayed in
491 the form of box-and-whisker plots allowing us to evaluate the median values and the
492 extrema (minimum and maximum). For both temperature and precipitation, medians
493 seem improved from GCMs to downscaling simulations; but the range of extrema
494 does not show significant changes.

495 Seasonal evolution for the 6 sub-regions is examined and compared to
496 observations. We did not observe an obvious improvement in terms of monthly
497 correlation coefficient. But the RMSE is generally ameliorated in the downscaling
498 simulations, for both surface air temperature and precipitation.

499 We believe that the good general performance of downscaling simulations
500 resides (partly at least) in their higher resolution and the good representation of the
501 terrain. We select 25 representative stations to validate simulations. The terrain in
502 downscaling simulations is closer to the real topography; deviations of both
503 precipitation and temperature are reduced. We also developed a simple algorithm of
504 topographic correction to ameliorate surface air temperature at station level. It is
505 primarily destined to provide relevant information for climate impact studies. But it

506 goes to the idea that a refined description of the terrain was one of the vital factors
507 leading to the superiority of downscaling simulations (Giorgi et al. 2004).
508 Unfortunately, there is no simple algorithm possible of terrain correction for
509 precipitation.

510 This paper mainly focuses on the added-value of LMDZ4 in its regional
511 configuration in comparison to its drivers, outputs from GCMs. It is worth to note that
512 other validation works of LMDZ4 over East Asia were also reported with re-analyses
513 (ERA-40 or ERA-Interim) as drivers (Zou et al. 2010, Yang et al. 2015). Such
514 simulations, in the “perfect boundary condition” mode, did show a good model
515 performance of LMDZ4 in capturing both the sign and magnitude of temperature and
516 precipitation anomalies.

517 An inter-comparison is planned for our next works to understand errors in
518 regional simulations and attribute them to imperfections in either large-scale boundary
519 conditions or physical parametrizations in LMDZ4. Finally we need to point out that
520 the lack of a reliable observation dataset also contributes to uncertainties for
521 evaluating high-resolution climate models.

522

523

524 **Acknowledgments:**

525 This work is supported jointly by the National Natural Science Foundation of China
526 (Grant No. 41230528), National Program on Key Basic Research Project of China
527 (Grant No. 2012CB955204), China R&D Special Fund for Public Welfare Industry
528 (meteorology) (GYHY201306024) and a Project Funded by the Priority Academic
529 Program Development (PAPD) of Jiangsu Higher Education Institutions. Helpful
530 comments from the anonymous reviewers are greatly appreciated.

531

532 **References:**

533 Carril A, Menendez C, Remedio A, Robledo F, Sorensson A, Tencer B, Boulanger JP, de Castro M,
534 Jacob D, Le Treut H, Li L, Penalba O, Pfeifer S, Rusticucci M, Salio P, Samuelsson P, Sanchez
535 E, Zaninelli P (2012) Assessment of a multi-RCM ensemble for South America. *Climate
536 Dynamics*, 39, 2747-2768.

537 Chen D, Ou T, Gong L, Xu CY, Li W, Ho CH, Qian W (2010) Spatial interpolation of daily
538 precipitation in China: 1951-2005. *Adv Atmos Sci* 27(6) : 1221-1232. doi:
539 10.1007/s00376-010-9151-y

540 Chen W, Jiang Z, Li L, Yiou P (2011a) Simulation of regional climate change under the IPCC A2

541 scenario in southeast China, *Clim Dyn* 36: 491-507

542 Chen W, Jiang Z, Li L (2011b) Probabilistic projections of climate change over China under the
543 SRES A1B scenario using 28 AOGCMs, *J Clim* 24: 4741-4756. DOI:
544 10.1175/2011JCLI4102.1

545 Cosgrove, B. A., and Coauthors (2003) Real-time and retrospective forcing in the North American
546 Land Data Assimilation Systems (NLDAS) project. *J Geophys Res*, 108, 8842,
547 doi:10.1029/2002JD003118.

548

549 Deque M, Piedelievre JP (1995) High resolution climate simulation over Europe. *Clim Dyn* 11:
550 321-340

551 Dong M, Wu T, Wang Z (2013) Simulation of the Precipitation and Its Variation During the 20th
552 Century Using the BCC Climate Model (BCC_CSM1.0). *Journal of applied meteorological*
553 *science* 24(1):1-11 (in Chinese)

554 Dong L, Zhou T (2013) Steric sea level change in twentieth century historical climate simulation
555 and IPCC-RCP8.5 scenario projection: A comparison of two versions of the FGOALS model.
556 *Adv Atmos Sci* 30(3): 841-854, doi:10.1007/s00376-012-2224-3

557 Dufresne JL, and co-authors (2013) Climate change projections using the IPSL-CM5 Earth
558 System Model: from CMIP3 to CMIP5. *Climate Dynamics*, 40, 2123-2165. DOI:
559 10.1007/s00382-012-1636-1

560

561 Flato et al. (2013) IPCC AR5 Chapter 9: Evaluation of Climate Models.

562 Frei C, Schöll R, Fukutome S, Schmidli J, Vidale PL (2006) Future change of precipitation
563 extremes in Europe: Intercomparison of scenarios from regional climate models. *J Geophys*
564 *Res* 111: D06105 doi:10.1029/2005JD005965

565 Gao XJ, Xu Y, Zhao ZC (2006) On the role of resolution and topography in the simulation of east
566 Asia precipitation. *Theor. Appl. Climatol.*, 86: 173-185.

567 Gao XJ, Shi Y, Giorgi F. (2010) A high resolution simulation of climate change over China. *Sci*
568 *China Earth Sci* 40(7): 911-922 (in Chinese)

569 Gao XJ, Shi Y, Zhang DF (2012a) Climate change in China in the 21st century as simulated by a
570 high resolution regional climate model. *Chin Sci Bull* 57: 374-381. (in Chinese)

571 Gao XJ, et al (2012b) Uncertainties in monsoon precipitation projections over China: results from
572 two high-resolution RCM simulations. *Climate Research* 52: 213-226

573 Giorgi F, Bi X, Pal J.S. (2004) Mean, interannual variability and trends in a regional climate
574 change experiment over Europe. I. Present-day climate (1961-1990). *Climate Dynamics* 22:
575 733-756

576 Giorgi F, Jones C, Asrar GR. (2009) Addressing climate information needs at the regional level:
577 the CORDEX framework. *WMO Bulletin*, 58(3): 175-183.

578 Goubanova K, Li L (2007) Extremes in temperature and precipitation around the Mediterranean
579 basin in an ensemble of future climate scenario simulations. *Global and Planetary Change*
580 57:27-42

581 Guo Y, Li J, and Li Y (2012) A time-scale decomposition approach to statistically downscale
582 summer rainfall over North China. *J. Climate*, 25, 572-591.

583 Guo Y, Li J and Li Y (2014) Seasonal forecasting of North China summer rainfall using a
584 statistical downscaling model. *J. Appl. Meteor. Climatol.*, 53, 1739-1749

585 Hourdin F and co-authors (2006) The LMDZ4 general circulation model: climate performance and
586 sensitivity to parametrized physics with emphasis on tropical convection. *Climate Dynamics*,
587 27, 787-813.

588 IPCC (2007) Regional climate projection. *Climate Change 2007: The Physical Science Basis*.
589 Contribution of Working Group I to the Fourth Assessment Report of the Intergovernmental
590 Panel on Climate Change, S. Solomon et al., Eds., Cambridge University Press, Cambridge,
591 UK and New York, NY, USA,849-926.

592 Jiang D B, Tian Z P. (2013) East Asian monsoon change for the 21st century: Results of CMIP3
593 and CMIP5 models. *Chin Sci Bull*, 58, doi: 10.1007/s11434-012-5533-0

594 Jiang Z, Song J, Li L and Chen W (2012) Extreme climate events in China: IPCC-AR4 model
595 evaluation and projection, *Climatic Change* 110:385-401, doi: 10.1007/s10584-011-0090-0

596 Jiang Z, Li W, Xu J and Li L (2015) Extreme Precipitation Indices over China in CMIP5 models.
597 Part 1: Models evaluation. *J Climate*. 28, 8603–8619.

598 Kitoh A, H Endo, Kumar K, et al (2013) Monsoons in a changing world: A regional perspective in
599 a global context. *J Geophys Res Atmos*, 118, 3053-3065, doi: 10.1002/jgrd.50258.

600 Le Treut H, Li Z, Forichon M (1994) Sensitivity of the LMD general circulation model to
601 greenhouse forcing associated with two different cloud water parameterizations. *J Clim* 7:
602 1827-1841

603 L'Hévéder B, Li L, Sevault F, Somot S (2013) Interannual variability of deep convection in the
604 Northwestern Mediterranean simulated with a coupled AORCM. *Climate Dynamics*, 41,
605 937-960.

606 Li H, Feng L, and Zhou T (2011) Multi-model projection of July-August climate extreme changes
607 over China under CO2 doubling. Part I: Precipitation. *Adv Atmos Sci.*, 28(2), 433-447,
608 doi:10.1007/s00376-010-0013-4

609 Li L, Lin P, Yu Y, et al, (2013) The Flexible Global Ocean-Atmosphere-Land System Model:
610 Version g2: FGOALS-g2. *Atmos. Adv. Sci.* 30(3):543-560

611 Li Z (1999) Ensemble atmospheric GCM simulation of climate interannual variability from 1979
612 to 1994. *J Clim* 12:986-1001

613 Li Z (2006) Atmospheric GCM response to an idealized anomaly of the Mediterranean sea surface
614 temperature. *Climate Dynamics*, 27, 543-552.

615 Mannig B, Müller M, Starke E, Merckenschlager C, Mao W, Zhi X, Podzun R, Jacob D, Paeth H
616 (2013) Dynamical downscaling of climate change in Central Asia. *Glob Planet Change*
617 110:26-39

618 Rojas M, Li LZ, Kanakidou M, Hatzianastassiou N, Seze G, Le Treut H (2013) Winter weather
619 regimes over the Mediterranean region: their role for the regional climate and projected
620 changes in the 21st century. *Climate Dynamics*, 41, 551-571.

621 Shi Y, Gao X, Wu J, Giorgi F (2011) Changes in snow cover over China in the 21st century as
622 simulated by a high resolution regional climate model. *Environ Res Lett* 6,
623 doi:10.1088/1748-9326/6/4/045401

624 Solman S, Sanchez E, Samuelsson P, da Rocha R, Li L, Marengo J, Pessacg N, Remedio ARC,
625 Chou SC, Berbery H, Le Treut H, de Castroand M, Jacob D (2013) Evaluation of an
626 ensemble of regional climate model simulations over South America driven by the
627 ERA-Interim reanalysis: Model performance and uncertainties. *Climate Dynamics*, 41,
628 1139-1157

629 Sperber KR, Annamalai H, Kang I-S, Kitoh A, Moise A, Turner A, Wang B, Zhou T (2013) The
630 Asian summer monsoon: an intercomparison of CMIP5 vs. CMIP3 simulations of the late 20th
631 century. *Clim Dyn* 1-34, doi: 10.1007/s00382-012-1607-6

632 Taylor KE, Stouffer RJ, Meehl GA (2012) An overview of CMIP5 and the experiment design. *Bull*
633 *Am Meteorol Soc* doi:10.1175/BAMS-D-11-00094.1

634 Tippet MK, Barlow M, Lyon B (2003) Statistical correction of central southwest Asia winter
635 precipitation simulations. *Int J Climatol* 23, 1421–1433.

636 van Vuuren DP, Edmonds J, Kainuma M, Riahi K, Thomson A, Hibbard K, Hurtt GC, Kram T, et
637 al (2011) The representative concentration pathways: an overview. *Climatic Change* 109:5-31

638 Vautard R, Noël T, Li L, Vrac M, Martin E, Dandin P, Cattiaux J, Joussaume S (2013) Climate
639 variability and trends in downscaled high-resolution simulations and projections over
640 Metropolitan France. *Climate Dynamics*, 41, 1419-1437.

641 Wang S, Yu E (2013) Dynamical downscaling simulation over China using the nested
642 MIROC/WRF model. *Climatic and Environmental Research* 18 (6): 681–692. (in Chinese)

643 Wu T, Li W, Ji J, Xin X, Li L, Zhang F, Wei M, Shi X (2013) Global carbon budgets simulated by
644 the Beijing Climate Center Climate System Model for the last century. *J Geophys Res Atmos*
645 118, 1-22, doi:10.1002/jgrd.50320

646 Xu Y, Gao X, Shen Y (2009) A daily temperature dataset over China and its application in
647 validating a RCM simulation. *Adv Atmos Sci* 26(4): 763-772

648 Xu Y, Xu C. (2012) Preliminary assessment of simulations of climate changes over China by
649 CMIP5 multi-models. *Atmospheric and Oceanic Science Letters*, 5: 489-494.

650 Yang H, Jiang ZH, Li L (2015) Simulation of the East Asian Summer Climate with a Variable
651 Resolution Model LMDZ4. *Transactions of Atmospheric Sciences (in Chinese)*

652 You Q, Fraedrich K, Ren G, Ye B, Meng X, Kang S (2012) Inconsistencies of precipitation in the
653 eastern and central Tibetan Plateau between surface adjusted data and reanalysis. *Theor Appl*
654 *Climatol* 109:485-496.

655 Yu Y, He J, Zheng W, Luan Y (2013) Annual Cycle and Interannual Variability in the Tropical
656 Pacific by three versions of FGOALS. *Adv Atmos Sci* 30(3):621-637,
657 doi:10.1007/s00376-013-2184-2

658 Zhang D, Shi Y (2012) Numerical simulation of Climate Changes over North China by the
659 RegCM3 model. *Chinese J. Geophys*, 55(9):2854-2866. (in Chinese)

660 Zhang J, L Li, T J Zhou, and X.G. Xin (2013) Evaluation of Spring Persistent Rainfall over East
661 Asia in CMIP3/CMIP5 AGCM simulations. *Advances in Atmospheric Science*. 30(6):
662 1587-1600

663 Zhao T, Guo W, Fu C (2008) Calibrating and evaluating reanalysis surface temperature error by
664 topographic correction. *J Clim*, 21:1440-1446.

665 Zhou T, Li Z (2002) Simulation of the East Asian summer monsoon using a variable resolution
666 atmospheric GCM. *Clim Dyn* 19: 167-180

667 Zhou T, and Yu R (2006) Twentieth century surface air temperature over China and the globe
668 simulated by coupled climate models. *J. Climate*, 19, 5843-5858.

669 Zhou T, Song F, Chen X (2013) Historical evolution of global and regional surface air temperature
670 simulated by FGOALS-s2 and FGOALS-g2: How reliable are the model results? *Adv Atmos*
671 *Sci* 30(3): 638-657

672 Zhou T, Chen X, Dong L, et al. (2014) Chinese contribution to CMIP5: An overview of five
673 Chinese models' performances. *J Meteor Res*, 28(4), 481-509.

674 Zou L, Zhou T, Li Z, et al. (2010) East China Summer Rainfall Variability of 1958-2000:
675 Dynamical Downscaling with a Variable-Resolution AGCM. *J. Climate*, 23:6394-6408

676

677

678 **Table Captions**

679 **Table 1** Sources of models and data

680 Table 2 Correlation coefficients and root-mean-square error (RMSE) (unit: mm/day)
681 to measure the seasonal match between the observed and simulated precipitations for
682 six sub-regions in China and three pairs of global/regional simulations. Figures in
683 bold in the regional simulation columns indicate improvement (higher correlation or
684 lower RMSE) compared to their counterparts in global models.

685 **Table 3** Weather stations details: EL (m) is the elevation of station; ΔEL (m), ΔT
686 ($^{\circ}C$) and ΔPr (%) are the differences of model elevation, simulated temperature and
687 precipitation with the true terrain, observed temperature and precipitation,
688 respectively. ΔT -cor ($^{\circ}C$) is the same as ΔT ($^{\circ}C$), but for topography-corrected
689 temperature. GCM-ave stands for the average of BCC, FGOALS and IPSL, RCM-ave
690 stands for the average of LMDZ/BCC, LMDZ/FGOALS and LMDZ/IPSL. Figures in
691 bold in the regional simulation columns indicate improvement compared to their
692 counterparts in global models.

693

694 **Figure Captions**

695 **Fig.1** Grid (in the form of mosaic) and surface orography (bottom color shading in m)
696 of models (a) LMDZ, (b) BCC, (c) FGOALS, (d) IPSL in East Asia

697 **Fig.2** Distribution of annual-mean temperature ($^{\circ}C$) during 1961-2005 from
698 observation (top), GCMs (middle row, BCC, FGOALS, IPSL) and downscaling
699 simulations (bottom row, LMDZ/BCC, LMDZ/FGOALS, LMDZ/IPSL) over China.
700 Spatial-pattern correlation coefficients and root-mean-square error (RMSE) between
701 the observed and simulated fields are given in panels a and b.

702 **Fig. 3** Same as Fig. 2, but for precipitation (mm/day).

703 **Fig. 4** Seasonal evolution of Spatial-pattern (a, b) correlation coefficients and (c, d)
704 root-mean-square error (RMSE) between the observed fields and simulated ones for (a,
705 c) temperature and (b, d) precipitation.

706 **Fig. 5** Long-term trend of annual-mean temperature (units: $^{\circ}C \cdot (a)^{-1}$, stippling
707 indicates areas where the trend is statistically significant at the 95% confidence level).
708 The layout of panels is the same as in Fig. 2: observation on the top, GCMs in the
709 middle and downscaling simulations on the bottom.

710 **Fig. 6** Same as Fig. 5, but for long-term trend of annual precipitation (units:
711 $(mm/d) \cdot (a)^{-1}$, stippling indicates areas where the trend is statistically significant at the
712 95% confidence level).

713 **Fig. 7** Distribution of annual temperature during 1961-2005 for different data sets and
714 different regions. These, box and whisker plots show the median (“+”), inter-quartile
715 range, maximum and minimum of temperatures respectively (unit: °C).

716 **Fig. 8** Same as Fig. 7, but for the annual precipitation (unit: mm/day).

717 **Fig.9** Seasonal cycle of monthly-mean temperature (°C) during 1961-2005 for
718 different data sets and different regions.

719 **Fig. 10** Same as Fig. 9, but for the seasonal cycle of precipitation (mm/day).

720 **Fig. 11** Geographic positions of the 25 representative stations in China

721 **Fig. 12** Climatological mean of geopotential height at 500 hPa (contours, unit: dagpm)
722 and winds at 850 hPa (vectors, unit: m/s) for (a,d) ERA-interim and biases in (b,e)
723 GCMs-ave and (c,f) RCMs-ave (a, b, c for summer, d, e, f for winter).

724

Table1 Sources of models and data

	Data	Source	Time	Resolution
Model	LMDZ4	France, LMD	1961-2005	0.6×0.6
	BCC-csm1-1-m	China, BCC	1961-2005	1.125×1.125
	FGOALS-g2	China, IAP	1961-2005	2.8125×2.8125
	IPSL-CM5A-MR	France, IPSL	1961-2005	2.5×1.2676
Obs	Precipitation	Chen et al, 2010	1961-2005	0.5×0.5
	Temperature	Xu et al, 2009	1961-2005	0.5×0.5
	Elevation	China, CMA		Station

728 Table 2. Correlation coefficients and root-mean-square error (RMSE) (unit: mm/day) to measure
 729 the seasonal match between the observed and simulated precipitations for six sub-regions in China
 730 and three pairs of global/regional simulations. Figures in bold in the regional simulation columns
 731 indicate improvement (higher correlation or lower RMSE) compared to their counterparts in
 732 global models.

	BCC	LMDZ/ BCC	FGOALS	LMDZ/ FGOALS	IPSL	LMDZ/ IPSL
	Corr (RMSE)	Corr (RMSE)	Corr (RMSE)	Corr (RMSE)	Corr (RMSE)	Corr (RMSE)
NE	0.97 (0.58)	0.94 (0.82)	0.97 (0.58)	0.96 (0.66)	0.99 (0.91)	0.95 (0.69)
NC	0.96 (0.42)	0.96 (0.35)	0.93 (0.90)	0.97 (0.40)	0.97 (0.31)	0.96 (0.37)
YZ	0.86 (1.21)	0.90 (0.93)	0.85 (0.89)	0.86 (1.09)	0.95 (0.75)	0.94 (0.65)
SE	0.97 (1.87)	0.97 (1.46)	0.85 (1.83)	0.98 (1.01)	0.83 (1.74)	0.93 (1.30)
NW	0.86 (0.76)	0.83 (0.40)	0.82 (0.99)	0.68 (0.51)	0.95 (0.47)	0.94 (0.39)
SW	0.93 (1.71)	0.86 (0.89)	0.97 (1.46)	0.92 (0.64)	0.97 (1.25)	0.98 (0.83)

733

734

735

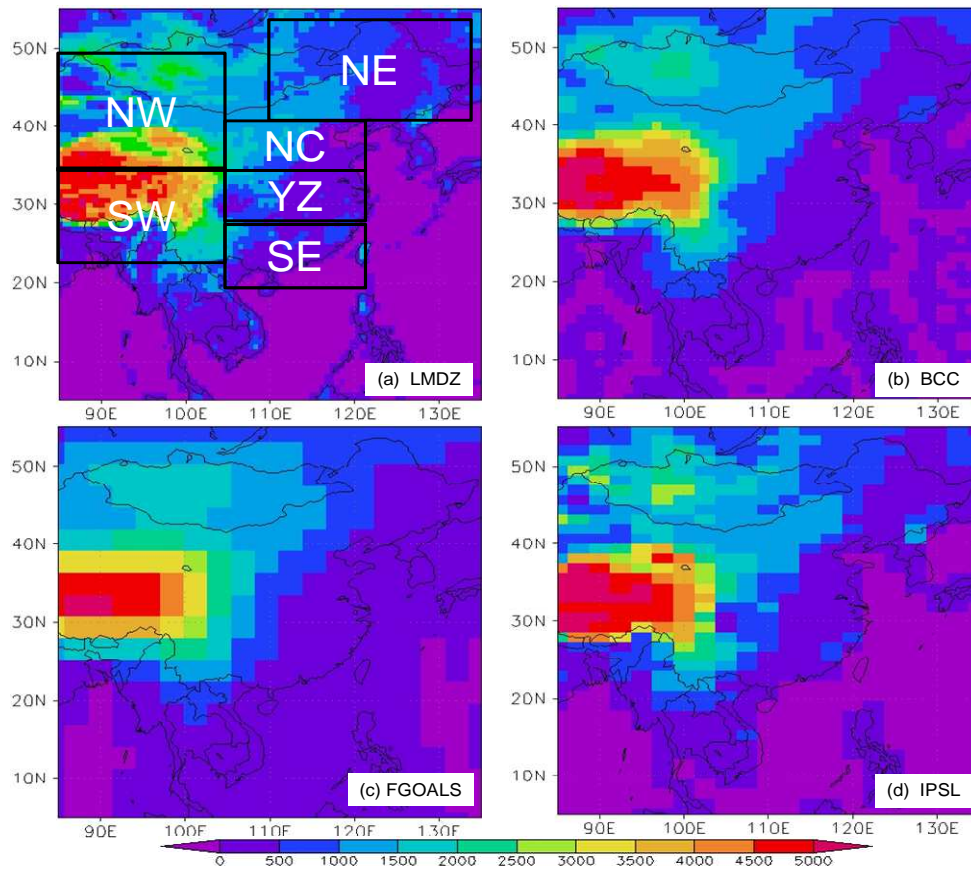
736 Table 3 Weather stations details: EL (m) is the elevation of station; Δ EL (m), Δ T ($^{\circ}$ C) and Δ Pr
737 (%) are the differences of model elevation, simulated temperature and precipitation with the true
738 terrain, observed temperature and precipitation, respectively. Δ T-cor ($^{\circ}$ C) is the same as Δ T($^{\circ}$ C),
739 but for topography-corrected temperature. GCM-ave stands for the average of BCC, FGOALS and
740 IPSL, RCM-ave stands for the average of LMDZ/BCC, LMDZ/FGOALS and LMDZ/IPSL.
741 Figures in bold in the regional simulation columns indicate improvement compared to their
742 counterparts in global models.

Sta.	EL (m)	Δ EL(m)				Δ T($^{\circ}$ C)		Δ T-cor($^{\circ}$ C)		Δ Pr(%)	
		BCC	FGOALS	IPSL	LMDZ	GCM -ave	RCM -ave	GCM -ave	RCM -ave	GCM -ave	RCM -ave
1 Harbin	142	129	245	139	63	-2.83	-0.37	-1.72	0.01	35	-7
2 Shenyang	49	187	247	86	48	-2.29	-0.47	-1.17	-0.18	7	-21
3 Chifeng	568	65	199	154	-30	-2.73	0.18	-1.82	0.08	68	2
4 Hohhot	1063	319	30	289	265	-2.29	-1.69	-0.90	-0.39	9	-38
5 Beijing	31	596	811	562	328	-5.28	-2.40	-1.01	-0.92	23	10
6 Jinan	170	-127	107	-24	10	-2.52	-0.48	-2.61	-0.42	-7	-18
7 Nanjing	7	46	102	50	92	-1.10	-0.25	-0.67	0.30	-2	-1
8 Hankou	23	103	263	127	39	-1.44	1.00	-0.37	1.24	-23	-38
9 Fuzhou	84	247	186	173	439	0.27	-0.98	1.59	1.66	-10	-5
10 Nanchang	47	166	239	249	-4	-1.64	0.50	-0.22	0.48	-36	-31
11 Changsha	68	140	316	203	41	-1.28	0.93	0.15	1.18	-40	-36
12 Guangzhou	41	114	196	155	13	-0.91	-0.03	0.10	0.05	-36	-34
13 Nanning	122	155	257	192	71	-0.80	-0.57	0.51	-0.15	-38	-9
14 Guizhou	1224	-173	-251	-158	215	1.47	-0.71	0.21	0.58	-19	-22
15 Chongqing	351	201	767	383	66	-3.08	1.32	-0.15	1.72	-25	-64
16 Chengdou	506	1492	1467	-61	27	-5.40	0.87	0.88	1.04	18	-65
17 Xichang	1591	795	537	772	652	-0.83	-1.67	3.73	2.24	10	-39
18 Kunming	1886	96	-678	146	125	0.59	-1.02	-0.36	-0.27	-8	-25
19 Lhasa	3649	1200	185	1026	854	-5.35	-3.89	-0.12	1.23	86	-65
20 Xi'an	397	631	598	578	685	-4.17	-2.33	-0.26	1.17	52	26
21 Lanzhou	1517	847	863	560	781	-3.85	-1.32	1.06	1.36	151	49
22 Yinchuan	1111	270	456	544	308	-3.48	-1.51	-0.73	0.33	77	15
23 Xining	2295	952	419	518	560	-3.54	-1.89	0.55	1.47	58	-7
24 Yushu	3681	915	533	1127	865	-3.08	-2.07	2.50	3.12	55	-43
25 Urumqi	935	245	337	-219	-214	1.88	4.17	2.67	2.89	2	-35
Absolute-Ave	862.3	408	412	340	272	2.53	1.13	1.09	0.98	35.8	28.2

743

744

745

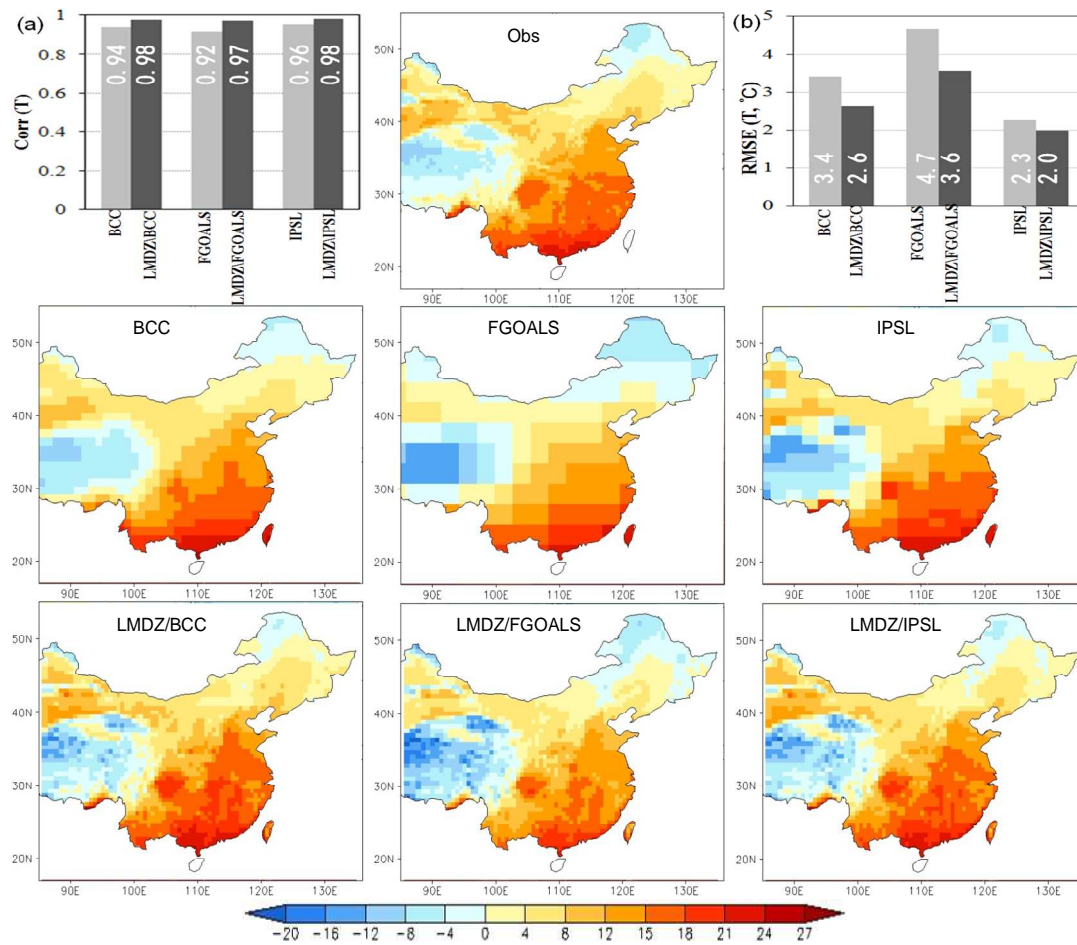


746

747 Fig.1. Grid (in the form of mosaic) and surface orography (bottom color shading in m) of models

748 (a) LMDZ, (b) BCC, (c) FGOALS, (d) IPSL in East Asia

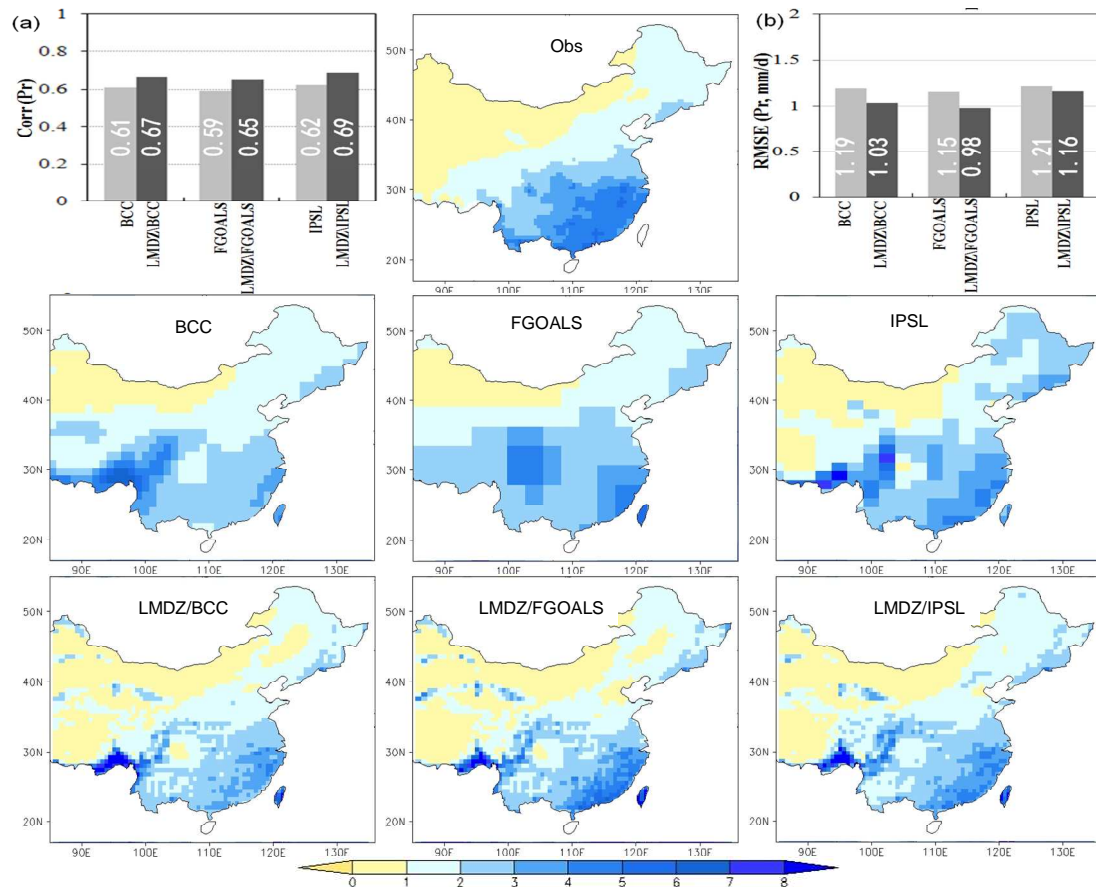
749



750

751 Fig. 2 Distribution of annual-mean temperature ($^{\circ}\text{C}$) during 1961-2005 from observation (top),
 752 GCMs (middle row, BCC, FGOALS, IPSL) and downscaling simulations (bottom row,
 753 LMDZ/BCC, LMDZ/FGOALS, LMDZ/IPSL) over China. Spatial-pattern correlation coefficients
 754 and root-mean-square error (RMSE) between the observed and simulated fields are given in
 755 panels a and b.

756



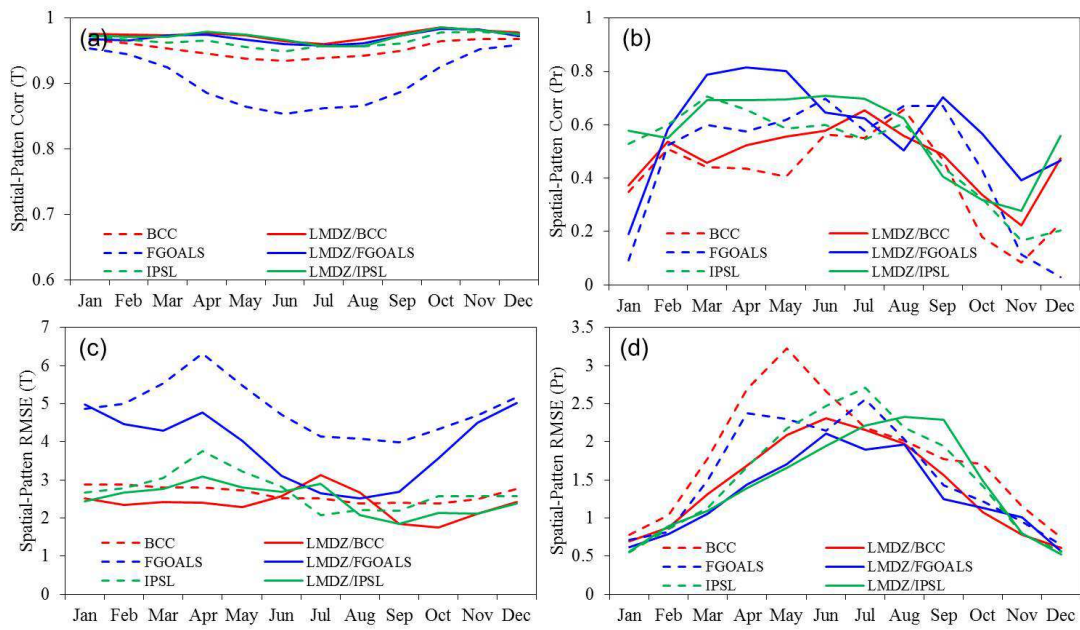
757

758 Fig. 3 Same as in Fig. 2, but for precipitation (mm/day).

759

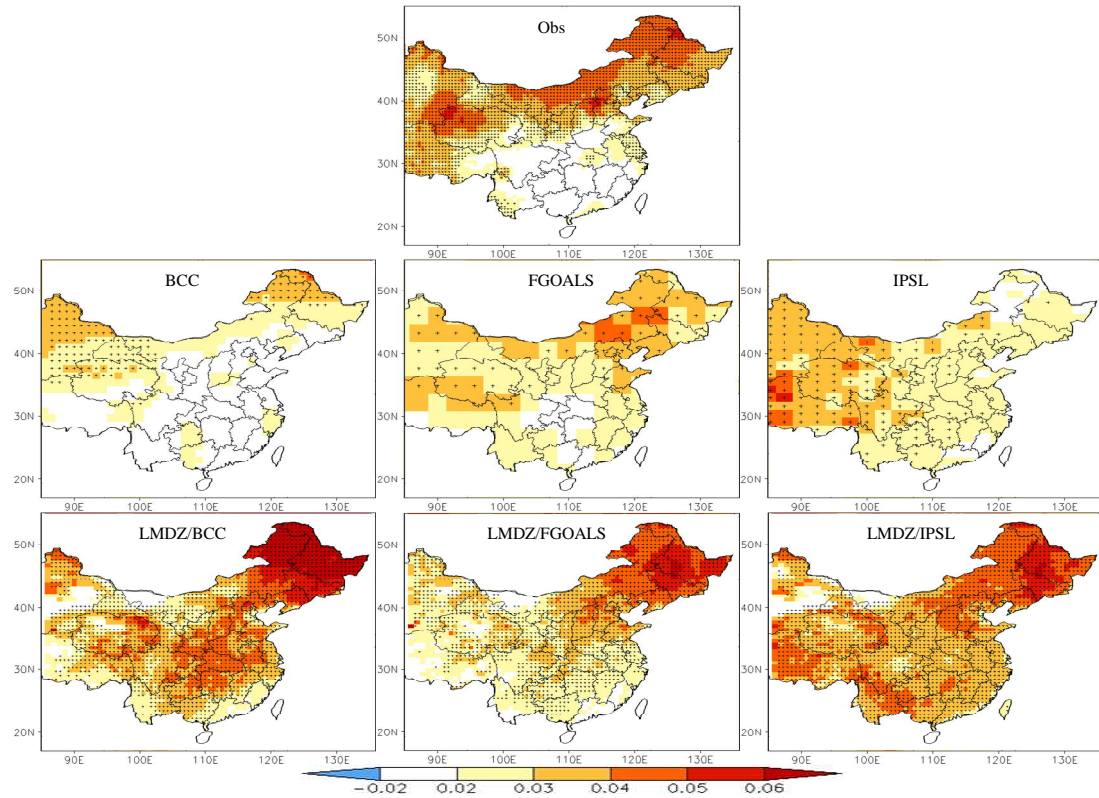
760

761



762

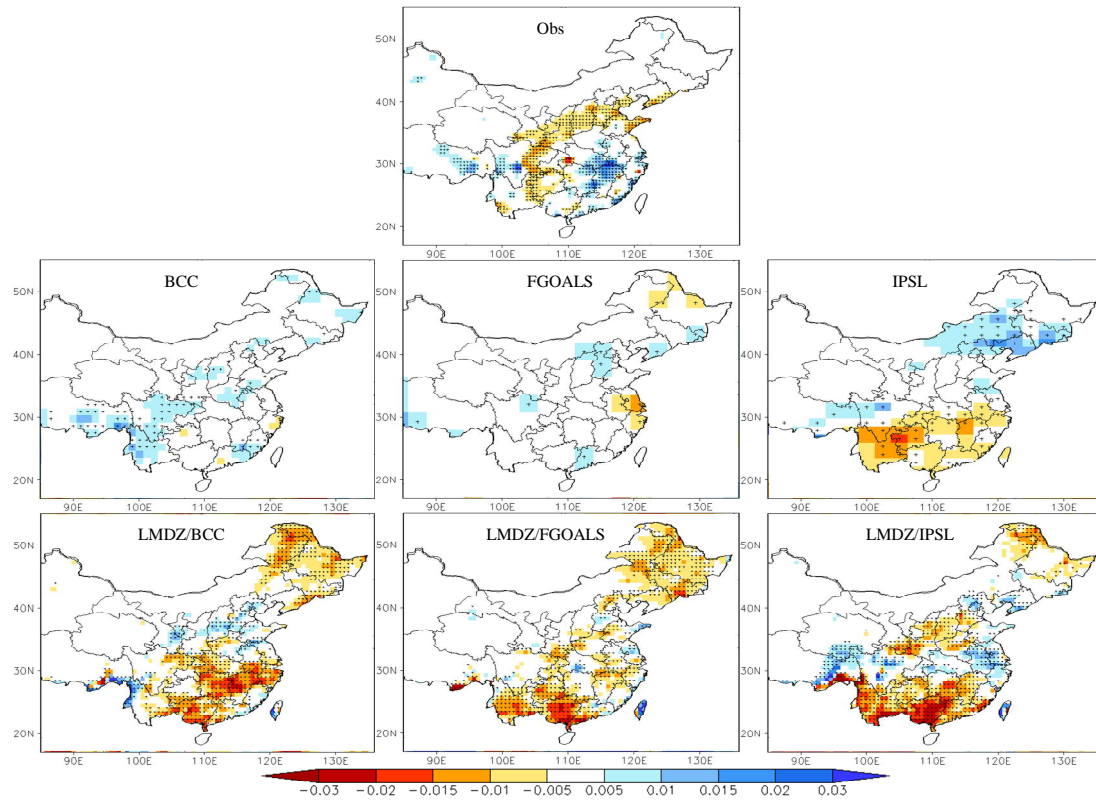
763 Fig.4 Seasonal evolution of Spatial-pattern (a, b) correlation coefficients and (c, d)
764 root-mean-square error (RMSE) between the observed fields and simulated ones for (a, c)
765 temperature and (b, d) precipitation.
766



767

768 Fig. 5 Long-term trend of annual-mean temperature (units: $^{\circ}\text{C}\cdot(\text{a})^{-1}$, stippling indicates areas
 769 where the trend is statistically significant at the 95% confidence level). The layout of panels is the
 770 same as in Fig. 2: observation on the top, GCMs in the middle and downscaling simulations on the
 771 bottom.

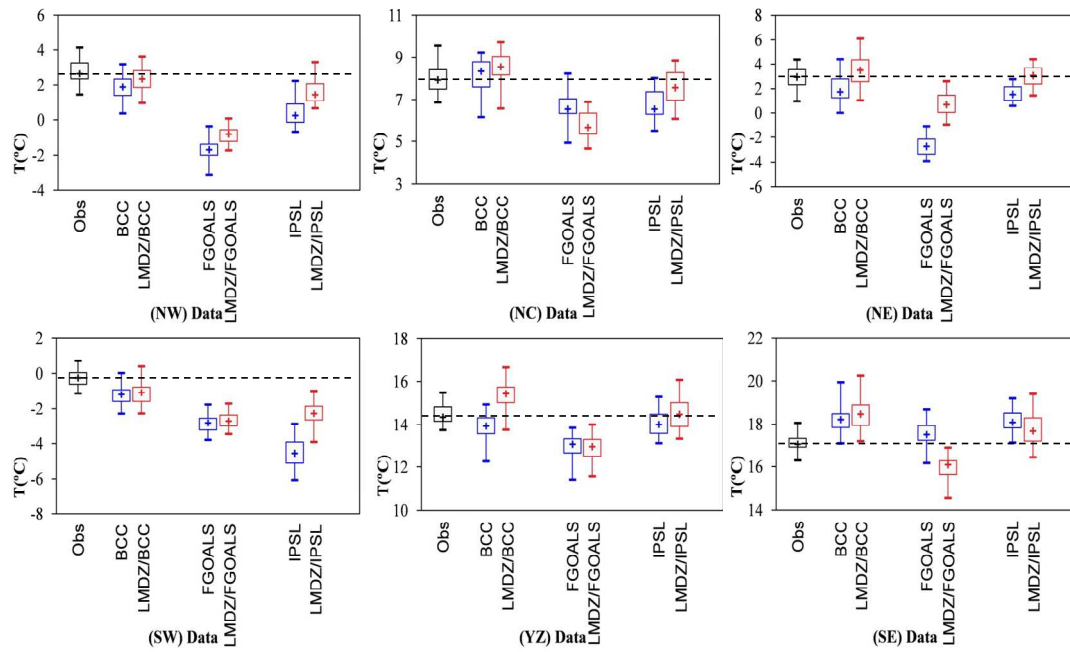
772



773

774 Fig. 6 Same as in Fig. 5, but for long-term trend of annual precipitation (units: $(\text{mm/d}) \cdot (\text{a})^{-1}$,
 775 stippling indicates areas where the trend is statistically significant at the 95% confidence level).

776



777

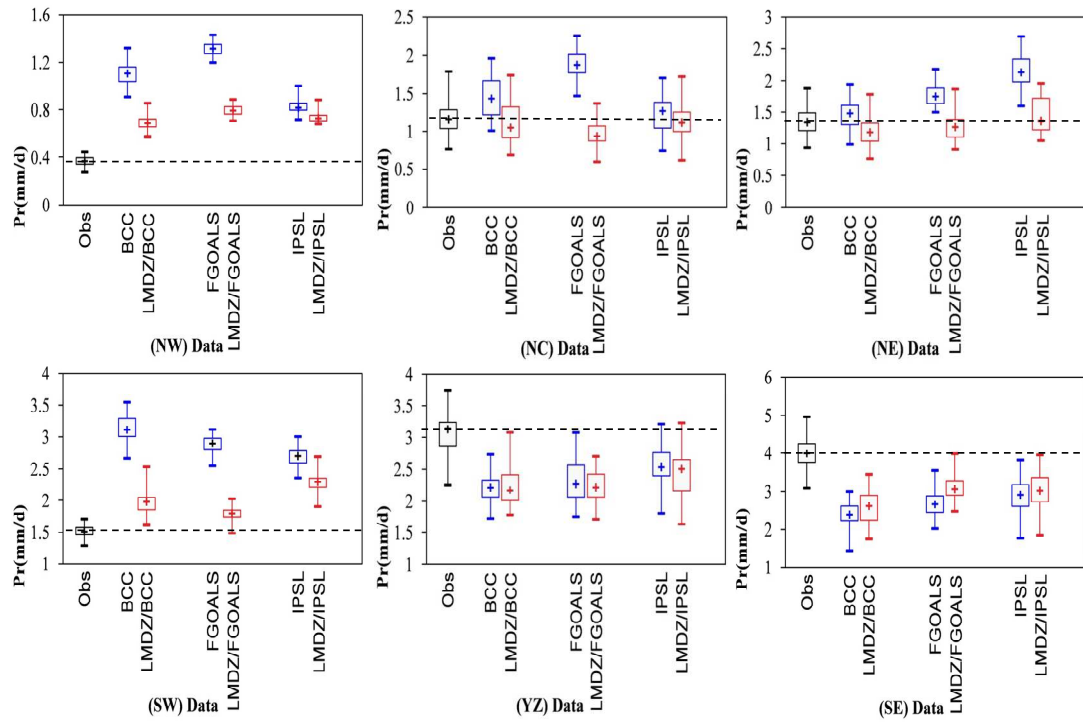
778 Fig. 7 Distribution of annual temperature during 1961-2005 for different data sets and different

779 regions. These box and whisker plots show the median (“+”), inter-quartile range, maximum and

780 minimum of temperatures respectively (unit: °C).

781

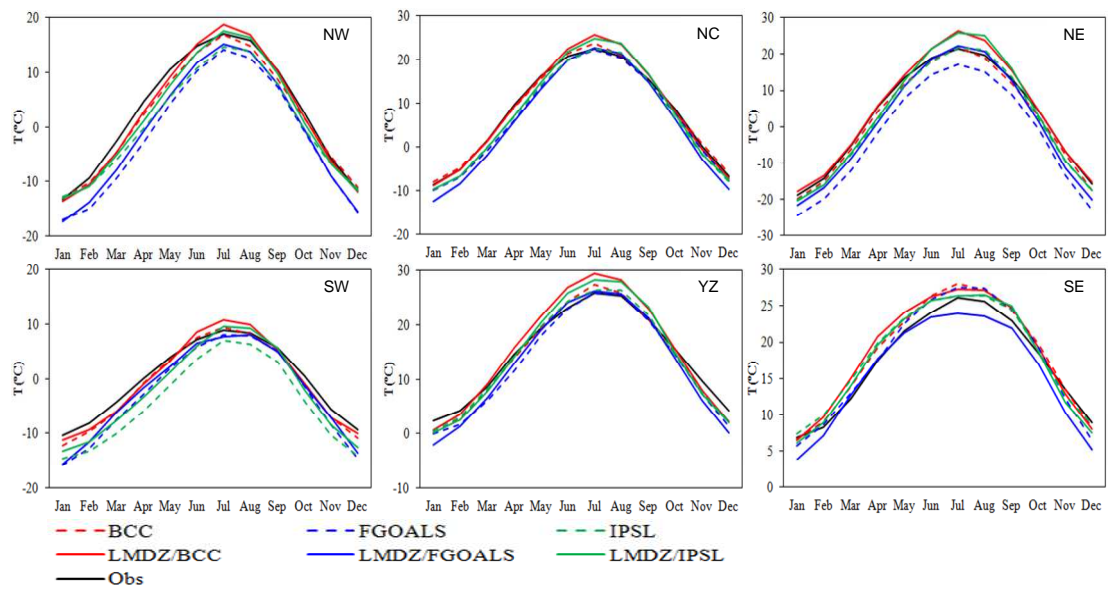
782



783

784 Fig. 8 Same as in Fig. 7, but for the annual precipitation (unit: mm/day).

785

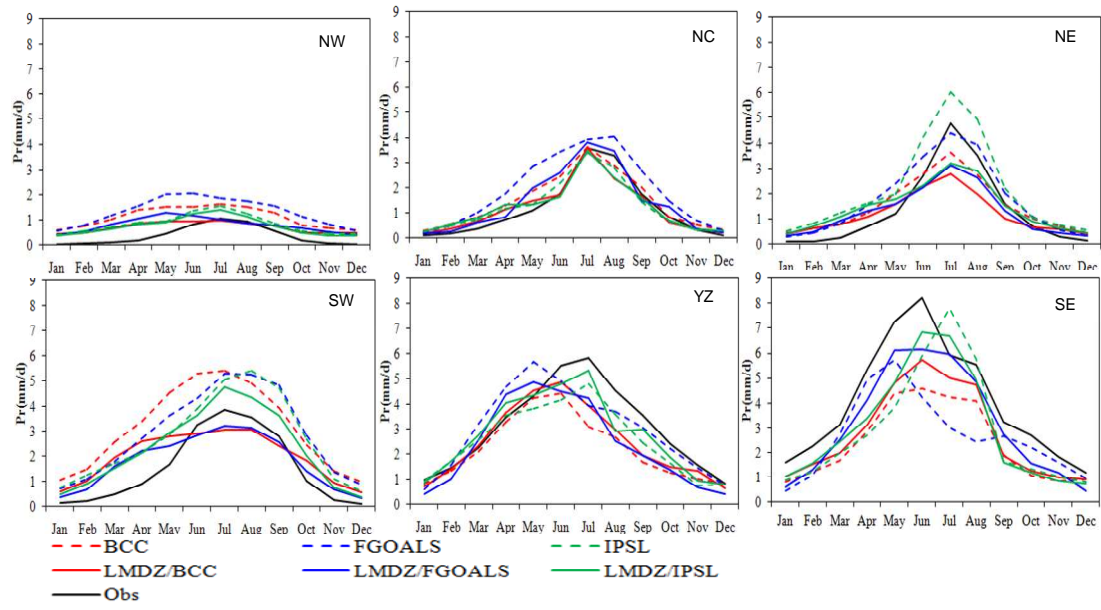


786

787 Fig. 9 Seasonal cycle of monthly-mean surface air temperature (°C) during 1961-2005 for

788 different datasets and different regions.

789



790

791 Fig. 10. Same as in Fig. 9, but for precipitation (mm/day).

792

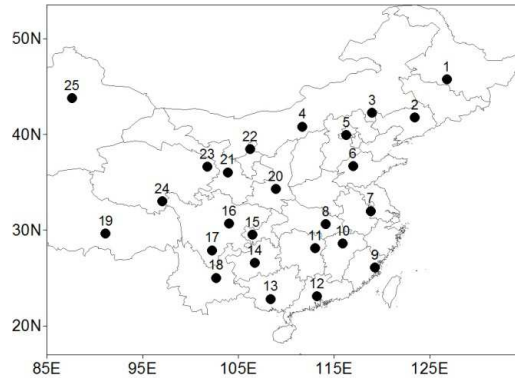
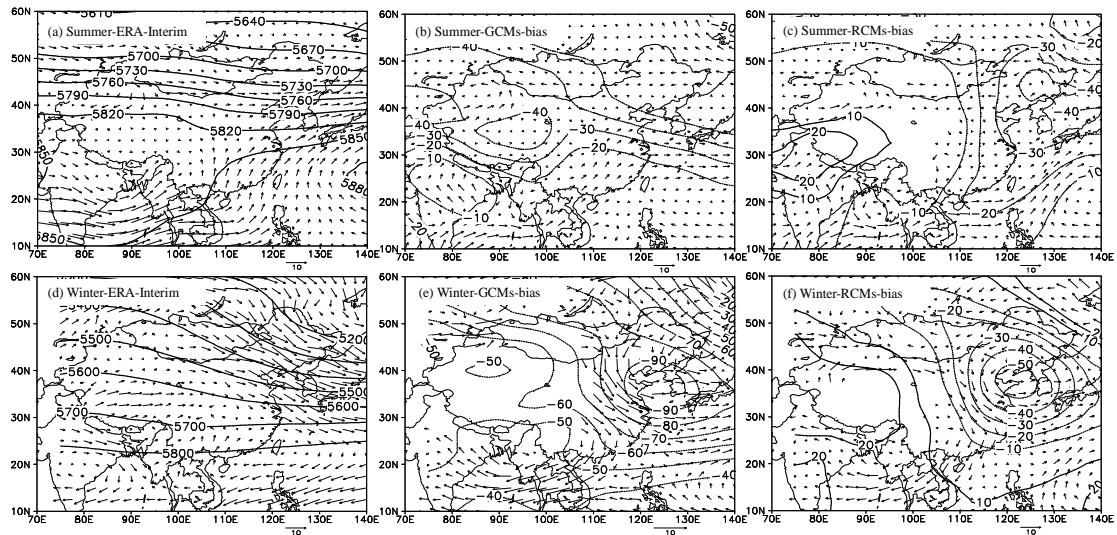


Fig. 11. Geographic positions of the 25 representative stations in China

793
794
795



796

797 Fig. 12. Climatological mean of geopotential height at 500 hPa (contours, unit: dagpm) and winds
 798 at 850 hPa (vectors, unit: m/s) for (a,d) ERA-interim and biases in (b,e) GCMs-ave and (c,f)
 799 RCMs-ave (a, b, c for summer, d, e, f for winter).

800